Hollow porous carbon confined atomically ordered $PtCo_3$ intermetallic for efficient oxygen reduction reaction

Yezhou Hu[a], Xuyun Guo[a], Tao Shen[b], Ye Zhu*[a], Deli Wang*[b]

[a] Department of Applied Physics, Research Institute for Smart Energy, The Hong Kong Polytechnic University, Hung Hom, Hong Kong, China

[b]Key Laboratory of Material Chemistry for Energy Conversion and Storage (Huazhong University of Science and Technology), Ministry of Education, Hubei Key Laboratory of Material Chemistry and Service Failure, School of Chemistry and Chemical Engineering, Huazhong University of Science and Technology, Wuhan 430074, P. R. China

* Corresponding author

E-mail: yezhu@polyu.edu.hk (Ye Zhu), wangdl81125@hust.edu.cn (Deli Wang)

KEYWORDS: Fuel cells; Hollow porous structure; Atomically ordered structure; Intermetallic electrocatalyst; Carbon encapsulation

ABSTRACT: PtM_3 alloys have demonstrated superior oxygen reduction reaction (ORR) activity due to the strong strain effect caused by non-noble metal cores. However, the serious corrosion of non-noble metals in acid solution is still challenging. Herein, a hollow porous N-doped carbon sphere encapsulated $PtCo_3$ intermetallic electrocatalyst (*O*-$PtCo_3$@HNCS) is successfully prepared through Co pre-embedding and subsequent impregnation-reduction method. The Co pre-embedding step is responsible for the formation of abundant mesopores, and the subsequent impregnation-reduction process leads to the Pt-Co ordering and carbon encapsulation. Benefiting from the accelerated

mass transfer process, enhanced metal interaction and physical confinement effect, *O*-$PtCo_3$@HNCS exhibits excellent ORR activity and durability with negligible half-wave loss after long-term stability test in acid solution. The ordered $PtCo_3$ nanoparticles tightly anchored in the carbon matrix without obvious aggregation, sintering and agglomeration, responsible for the superior durability. The strategy for the carbon confinement in this work paves the way for achieving highly efficient catalysts with low Pt content, which can be used in various energy-related systems.

Introduction

Proton exchange membrane fuel cells (PEMFCs) have been considered as one of the most promising candidates for replacing traditional fossil fuel with renewables.[1] However, the sluggish oxygen reduction reaction (ORR) and high cost of Pt are the two major obstacles that hinder its application. While tremendous efforts have been spent on the development of non-noble metal catalysts and metal-free catalysts, such as transition metal-nitrogen-carbon (M-N-C, M=Fe, Co and Cu et al.)[2-4] and carbon materials with various heteroatom doping,[5, 6] their ORR performances are still far from satisfactory, especially in acid medium where serious corrosion can happen. Thus, lowering the usage of Pt and tuning its electrocatalytic property are still urgent but challenging.[7, 8] Alloying transition metals with Pt can not only reduce the usage of Pt but also improve the ORR efficiency. Among various Pt-based bimetallic catalysts, Pt-Co and Pt-Ni are the most representative. For example, Stamenkovic and co-workers have reported Pt_3Ni nanoframes which showed unprecedented ORR activity in 0.1 M $HClO_4$.[9] Such enhanced ORR performance can be ascribed to the imposed strain from

the inner non-noble metal core on the spontaneously formed Pt-rich outer shell. Higher ORR activity resulting from the strong compressive strain in low-Pt alloys has also been suggested in other works.[10, 11] Strasser and co-workers have reported that, in acid electrolytes, $PtCo_3$ exhibits the highest ORR activity compared with Pt_3Co and PtCo, which is largely caused by the formation of favorable Co-rich core-Pt-rich shell structure.[10] However, considering the low dissolution potential and poor thermal stability of non-noble metals (Co and Ni et al.) in acid electrolytes, the strain effect on Pt-rich shells can be weakened with the leaching of non-noble metals, leading to the rapid loss of ORR performance.[12, 13] Thus, a fundamental challenge is how to avoid non-noble metal leaching from low-Pt content alloy catalysts to retain the strong strain effect during ORR.

To prevent the leaching of non-noble metals from Pt-based bimetallic alloys, one effective way is to transform disordered alloys into atomically ordered intermetallics to achieve stronger *d-d* orbital interactions.[14, 15] The associated problem is that the synthesis of intermetallics tends to be conducted at high temperature, which may reduce the exposure of active sites caused by sintering, aggregation and/or agglomeration.[16, 17] On the other hand, the degradation mechanism of Pt during stability test is studied in detail. During the operation, the ORR performance can be significantly degraded by Ostwald-ripening, coalescence, aggregation and/or detachment.[18] Especially for coalescence and aggregation and/or detachment, the movement of Pt nanoparticles is mainly responsible for the performance degradation.[19] Carbon encapsulation can be a promising way to avoid the above-mentioned problem during both synthesis and

electrochemical processes, but a great challenge remaining is how to achieve the balance between the activity and durability of encapsulated nanoparticles.[16, 20-23] In other words, could the activity be maintained, or even enhanced if possible, under the physicochemical protection of carbon shells?

Herein, we developed a strategy to achieve the atomic structure ordered $PtCo_3$ intermetallic confined in hollow porous N-doped carbon (*O*-$PtCo_3$@HNCS) with low-Pt content for ORR. During synthesis, pre-embedded Co nanoparticles are essential as they not only serve as Co precursors for the formation of carbon confined $PtCo_3$ intermetallic nanoparticles but also create abundant mesopores for accelerated mass transfer as evidenced by transmission electron microscopy (TEM), X-ray diffraction (XRD) and Brunauer–Emmett–Teller surface analysis. More emphasis is put on understanding the morphology and surface structure change under the protection of carbon 'armor' before and after the stability test through surface-sensitive CO stripping voltammetry. We show that carbon encapsulation can not only inhibit the oxidation of Co and particle growth during high-temperature synthesis, but also avoid Oswald ripening, aggregation and agglomeration during the electrochemical process. These results deepen the understanding on performance improvement mechanism of carbon encapsulation, and provide essential guidance for constructing carbon encapsulated nanoparticles for various applications.

Results and discussion

Structural characterization of catalysts

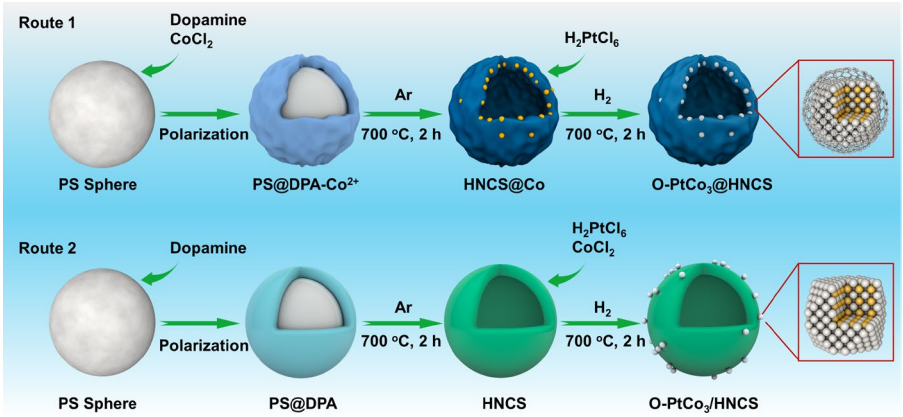

Figure 1. Schematic illustration of the synthesis of *O*-$PtCo_3$@HNCS (Route 1) and *O*-$PtCo_3$/HNCS (Route 2).

The synthesis of *O*-$PtCo_3$@HNCS is illustrated in **Figure 1** (route 1, see more details in supporting information). Briefly, Polystyrene (PS) spheres (~250 nm) were first obtained using emulsion method,[24] and then dispersed in Tris-buffer solution containing a certain amount of Co^{2+}. After fully mixing, dopamine (DPA) was added to above solution under vigorous stirring to achieve in situ polymerization on the surface of PS spheres. Benefiting from the strong chelating capability of DPA, DPA-Co^{2+} covering layers can be formed. Ultrafine Co nanoparticles confined in hollow N-doped carbon spheres (Co@HNCS) were obtained by annealing PS@DPA-Co^{2+} at 700 ^{o}C, during which the PS spheres serve as the sacrificial template and pore-forming agent (mainly micropores), and DPA layers provide confinement effect to prevent the overgrowth of Co nanoparticles.[25] The scanning electron microscopy (SEM) and TEM images of Co@HNCS revealed the achieved hollow structure with uniform distribution of Co nanoparticles. Co nanoparticles can be rarely observed on the surface, indicating no collapse of morphology and the successful embedding of Co nanoparticles in the hollow carbon matrix (**Figure S1** and **S2**). To achieve the formation of $PtCo_3$

nanoparticles and the subsequent disorder-order transformation, the Pt precursor reacted with Co@HNCS and was then deposited inside the hollow carbon matrix facilitated by the reducing-atmosphere and high-temperature annealing. For comparison, the ordered $PtCo_3$ nanoparticles supported on HNCS (denoted as *O*-$PtCo_3$/HNCS, **Figure 1**, route 2, see more details in supporting information) rather than embedded in HNCS, as well as carbon black (*O*-$PtCo_3$/C, with relatively weak metal-support interaction compared with that using N-doped carbon materials) were fabricated.

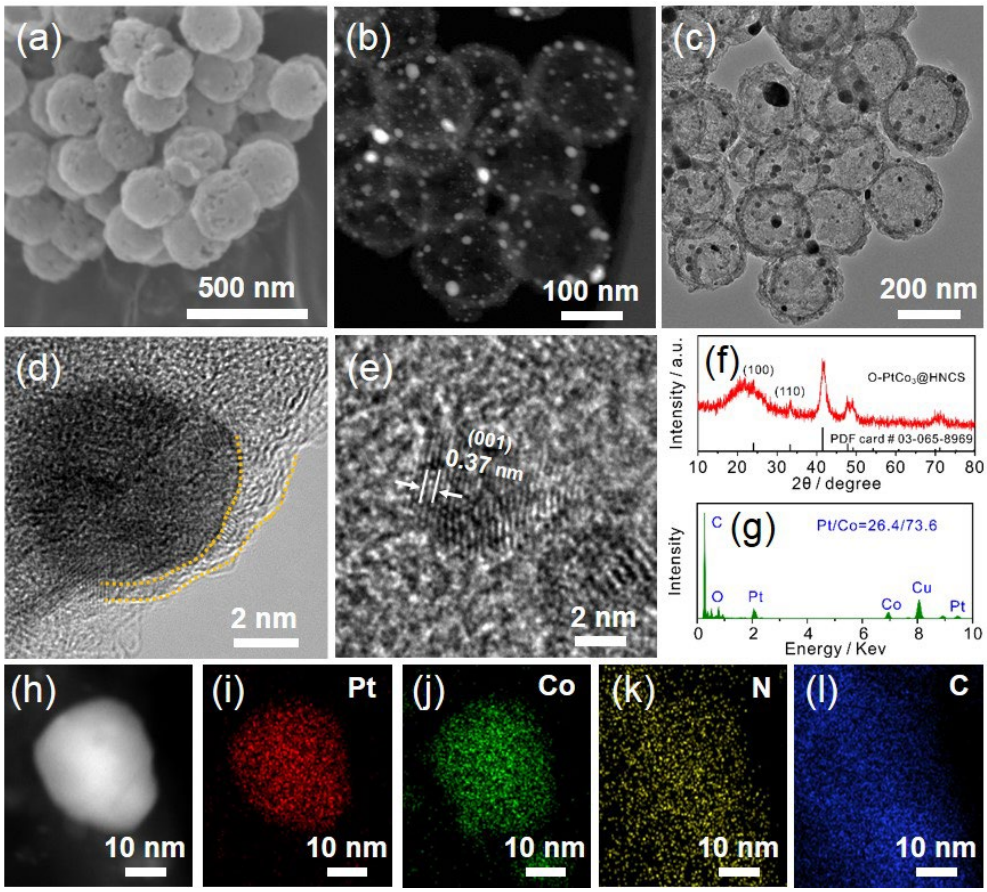

Figure 2. Morphology and structure characterization of *O*-$PtCo_3$@HNCS. (a) SEM, (b) dark-field, (c) bright-field TEM, and (d, e) HRTEM images of *O*-$PtCo_3$@HNCS. (f) XRD, (g) EDS and (h-l) corresponding EDS elemental maps of *O*-$PtCo_3$@HNCS/C.

The SEM image of *O*-$PtCo_3$@HNCS (**Figure 2a**) shows similar size and morphology to the Co@HNCS precursor (**Figure S1 and S2**), indicating good thermostability during high temperature synthesis. Interestingly, many mesopores (2-50 nm) are observed on the surface of *O*-$PtCo_3$@HNCS (but not on Co@HCNS, **Figure 2a** and **Figure S1**), which presumably results from the reaction between Co nanoparticles and Pt precursor during the impregnation and reduction process. The homogenous distribution of nanoparticles and the hollow structure with a shell thickness of ~20 nm is revealed from TEM images (**Figure 2b-c**). The ordered structure of $PtCo_3$ nanoparticles is confirmed by high-resolution TEM (**Figure 2e**), and XRD (**Figure 2f**), both showing the (001) superlattice fringes of ~0.37 nm.[11] Besides, the ordered atomic arrangement of O-$PtCo_3$@HNCS is further verified by the appearance of periodic bright Pt columns (with high Z-contrast) in HAADF-STEM image. (**Figure S3**) In **Figure 2g**, the energy-dispersive X-ray spectroscopy (EDS) shows that the ratio of Pt/Co is 26.4/73.6, which is close to the feed ratio. The corresponding EDS elemental maps (**Figure 2h-l**) further confirm the formation of N-doped carbon matrix and homogenous distribution of Pt and Co in *O*-$PtCo_3$@HNCS/C.

In contrast to the uniformly distributed nanoparticles in *O*-$PtCo_3$@HNCS, obvious clustering can be observed in *O*-$PtCo_3$/HNCS (**Figure S4a-b**). While for *O*-$PtCo_3$/C (**Figure S5a-b**), the inhomogeneous size distribution is even more obvious. To better compare the detailed surface structure of *O*-$PtCo_3$@HNCS and *O*-$PtCo_3$/HNCS, we utilized the backscattering electron (BSE) detector to acquire surface-sensitive images, simultaneously with ADF images from the transmitted signals in STEM. As shown in

Figure S6a-c, *O*-$PtCo_3$@HNCS exhibits a surface with only a few particles exposed outside the hollow carbon sphere, indicating that most of the *O*-$PtCo_3$ nanoparticles are fully encapsulated inside the carbon shell. This is consistent with TEM observation in **Figure 2d**, which shows a nanoparticle encapsulated by the carbon layer with the thickness of 1.3 nm (about 4-5 layer of carbon sheets). By contrast, the BSE image on *O*-$PtCo_3$/HNCS shows high-density nanoparticles along with agglomerated particles supported on the surface of the hollow carbon sphere without the protection of carbon shell (**Figure S6d-f**). This observation demonstrates that carbon confinement has been successfully achieved in *O*-$PtCo_3$@HNCS and can effectively prevent nanoparticles from migration or aggregation during high-temperature synthesis.

The N_2 adsorption/desorption test was conducted to investigate the impact of pre-embedding Co nanoparticles on specific surface area (SSA) and pore size distribution (PSD). The measured SSAs are respectively 494.8 and 253.3 m^2/g for *O*-$PtCo_3$@HNCS and *O*-$PtCo_3$/HNCS (**Figure S7a**), and the remarkable SSA enhancement in *O*-$PtCo_3$@HNCS suggests the increased number of micropores and mesopores. While both *O*-$PtCo_3$@HNCS and *O*-$PtCo_3$/HNCS deliver typical type-IV hysteresis (meaning micropores, mesopores and macropores co-exist),[26] the proportion of mesopores with the dominant pore size of 3.5 nm in *O*-$PtCo_3$@HNCS is much higher than that in *O*-$PtCo_3$/HNCS, as can be seen directly from the corresponding PSD profiles (**Figure S7b**). Raman spectra (**Figure S7c**) show that both *O*-$PtCo_3$@HNCS and *O*-$PtCo_3$/HNCS exhibit two typical peaks located at 1340 cm^{-1} (D band) and 1590 cm^{-1} (G band).[27] The higher I_D/I_G value (1.06) in *O*-$PtCo_3$@HNCS indicates that more defects

exist compared with that in *O*-$PtCo_3$/HNCS (0.96).[27] These results indicate that pre-embedding Co nanoparticles can not only provide a large number of micropores to achieve increased defects and exposure of active sites but also benefit the formation of accessible mesopores, the latter of which has been proven to effectively reduce mass-transfer resistance for ORR.[6]

XPS was performed to investigate the surface element composition and chemical bonding. **Figure S8** indicates the C 1s, N 1s and Co 2p XPS spectra of *O*-$PtCo_3$@HNCS. The spectrum of C 1s can be divided into four characteristic peaks located at 284.6, 285.3, 286.1 and 288.6 eV, which can be assigned to C-C/C=C, C-N, C-O and C=O bonds,[24] respectively. The N1s spectrum can also be deconvolved into four peaks for pyridinic N (398.4 eV), pyrrolic N (399.6 eV), graphitic N (400.9 eV) and oxidized N (402.7 V),[26] respectively. Our previous work has demonstrated the introduction of N into carbon matrix can greatly modify the electronic structure, thus providing much stronger interaction with the supported nanoparticles.[16, 21] The Co 2p spectra of *O*-$PtCo_3$@HNCS can be divided into several doublets, including Co^0 (778.4 and 793.7 eV), Co^{2+} (780.9 and 796.6 eV) and satellite peaks (785.8 and 802.7 eV). [28, 29] Notably, in Co 2p spectrum of *O*-$PtCo_3$/HNCS (**Figure S9**), nearly no characterized peak assigned to Co^0 can be detected, suggesting that carbon encapsulation in O-$PtCo_3$@HNCS can effectively prevent nanoparticles from oxidation.[30] This anti-oxidation property also ensures the maximal exposure of active sites, thus accelerating the ORR process. To further understand the important role of carbon encapsulation, the Pt 4f XPS spectra of *O*-$PtCo_3$@HNCS, *O*-$PtCo_3$/C and Pt/C are compared (**Figure S7d**).

A positive shift of 0.68 eV can be observed for *O*-$PtCo_3$/C compared with Pt/C. Usually, the shift of Pt 4f peaks to higher binding energy is associated with the weakened adsorption of oxygen-containing species on catalyst surfaces, thus approaching the top of activity volcano.[31] However, DFT calculation shows that alloying Co with Pt tends to cause excessively weakened OH adsorption, leading to decreased ORR activity.[32] In **Figure S7d**, the Pt 4f binding energy of *O*-$PtCo_3$@HNCS falls in between *O*-$PtCo_3$/C and Pt/C, which suggests that the excessively weakened OH adsorption in *O*-$PtCo_3$/C can be recovered to a certain degree after the introduction of N-doped carbon layer.

Electrochemical activities investigation

Electrocatalytic ORR activities were evaluated using CV and LSV techniques in 0.1 M $HClO_4$ solution. **Figure 3a** exhibits the CV curves of *O*-$PtCo_3$@HNCS, *O*-$PtCo_3$/HNCS and homemade Pt/C. Clear H adsorption/desorption regions can be observed in the potential range of 0.05-0.4 V.[14] Notably, much wider electrochemical double layers can be seen for *O*-$PtCo_3$@HNCS and *O*-$PtCo_3$/HNCS, which could be ascribed to the larger surface area of PS@DPA-(Co) derived hollow N-doped carbon support compared with carbon black.[27] Further, the LSV profiles of catalysts were recorded in O_2-saturated 0.1 M $HClO_4$ solution, as shown in **Figure 3b**. The ORR half-wave potential ($E_{1/2}$) of *O*-$PtCo_3$@HNCS (0.909 V) is much higher than that of *O*-$PtCo_3$/HNCS (0.882 V) and Pt/C (0.867 V). On the other hand, the enhanced ORR activity also implies that carbon encapsulation may not hamper the catalytic reaction. This can be verified from the calculated electron transfer number (n) as shown in **Figure S10**, meaning that the carbon encapsulation does not change the reaction route

(still 4-electrons pathway). **Figure 3c** shows the Tafel plots: In the high potential region, both *O*-$PtCo_3$@HCNS and *O*-$PtCo_3$/HNCS exhibit much higher log j_k values than Pt/C, suggesting their higher intrinsic activity. Whereas in low potential region, we can find that the log j_k value of *O*-$PtCo_3$/HNCS is almost equal to that of Pt/C, while *O*-$PtCo_3$@HNCS still exhibit the highest log j_k value, indicating the impeded mass transfer process for *O*-$PtCo_3$/HNCS due to the lack of mesopores. The decreased limiting current density of *O*-$PtCo_3$/HNCS in **Figure 3b** also confirms the limited mass-transfer process,[33] indicating that the Co nanoparticle pre-embedding plays a pivotal role in improving mass transfer process and ORR activity by creating abundant mesoporous structure in *O*-$PtCo_3$@HNCS.

To gain direct insight into the enhanced ORR activity of *O*-$PtCo_3$@HNCS, their mass activities (MA) and specific activities (SA) at 0.9 V were compared (**Figure 3d**). The calculated MA of *O*-$PtCo_3$@HNCS was 0.54 A mg^{-1}, 2.3 and 4.5 times that of *O*-$PtCo_3$/HNCS and Pt, even surpassing the DOE target (0.44 A mg^{-1}). The highest SA can also be observed in *O*-$PtCo_3$@HNCS. To further investigate the effect of structure ordering on ORR activity, contrast samples with disordered $PtCo_3$ nanoparticles confined in HNCS (*D*-$PtCo_3$@HNCS, 'D' indicates the disordered) were fabricated. **Figure S11** compares the ORR activities of *O*-$PtCo_3$@HNCS and *D*-$PtCo_3$@HNCS, showing a positive shift in $E_{1/2}$ that can be attributed to the downshift of *d*-band center associated with the structure ordering. Strong metal-support interaction (SMSI) has also been suggested to have a positive effect on ORR performance.[34] Thus, we further compared the ORR performance of *O*-$PtCo_3$/HNCS with that of *O*-$PtCo_3$/C. As shown

in **Figure S12**, even worse ORR activity can be observed for *O*-$PtCo_3$/HNCS with SMSI, implying that SMSI alone may not make up for the ORR activity loss caused by hindered mass transfer process. Overall, the enhanced ORR activity in *O*-$PtCo_3$@HNCS could be attributed to the combination of structure ordering, the SMSI, unique porous structure and fast electron transfer (mainly due to the close contact between carbon shell and encased nanoparticles[35]).

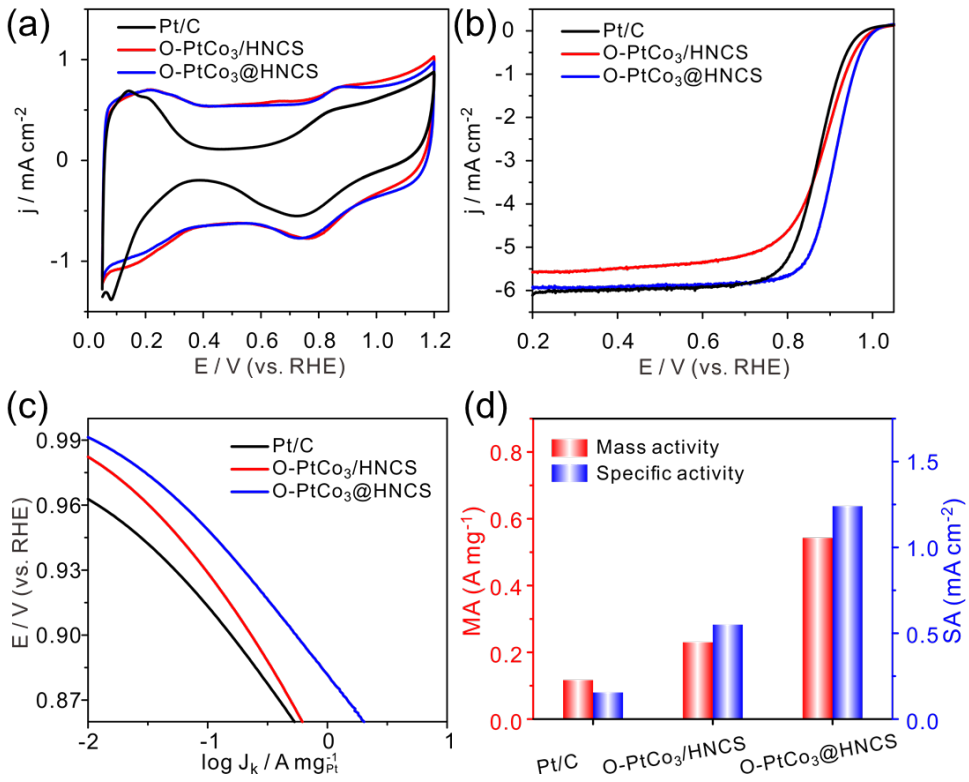

Figure 3. Electrocatalytic properties of Pt/C, *O*-$PtCo_3$/HNCS and *O*-$PtCo_3$@HNCS. (a) CV curves in Ar-saturated 0.1 M $HClO_4$ solution at room temperature, with a scan rate ~50 mV/s. (b) LSV curves in O_2-saturated 0.1 M $HClO_4$ solution at room temperature, with a scan rate ~10 mV/s. (c) Tafel plots, in which J_k is the kinetic current density. (d) Comparison of MA and SA at 0.9 V.

To evaluate the stability of *O*-$PtCo_3$@HNCS, *O*-$PtCo_3$/HNCS and Pt/C, the LSV profiles before and after different number of potentials cycles were compared as shown

in **Figure 4a** and **Figure S13a-b**. $E_{1/2}$ of *O*-$PtCo_3$@HNCS barely degrades with increasing potential cycles, indicating its superior stability. By contrast, the $E_{1/2}$ values of *O*-$PtCo_3$/HNCS and Pt/C degrade rapidly. The detailed $E_{1/2}$ attenuation rates are summarized in **Figure 4b**, with $E_{1/2}$ loss of 23 and 19 mV for *O*-$PtCo_3$/HNCS and Pt/C, while only ~1 mV for *O*-$PtCo_3$@HNCS. The changes in MA and SA at different potential stages are also calculated (**Figure 4c** and **Figure S14**). For *O*-$PtCo_3$@HNCS, a MA retention of 92.6% can be observed after 20,000 potential cycles, and the values for *O*-$PtCo_3$/HNCS and Pt/C are 78.3% and 41.7%, respectively. Such enhanced ORR stability could be ascribed to the protective 'carbon armor', which may greatly prevent the possible aggregation, detachment or dissolution during potential cycling. To better evaluate the ORR stability of the O-$PtCo_3$@HNCS and make a comparison with DOE target (<40% loss in MA after 30,000 cycles), the stability tests after 30,000 are recorded. A negligible loss in half-wave potential can be observed (**Figure 4d**). Besides, after 30,000 cycles, the loss in MA is only 9.9%, surpassing the DOE target on MA loss (<40%) (**Figure 4e**). This not only demonstrates the superior stability of O-$PtCo_3$@HNCS but also the great potential application in fuel cells.

Considering the three factors (SMSI, ordering and encapsulation) that may influence the catalytic stabilities, we further recorded the LSV profiles of *D*-$PtCo_3$@HNCS (**Figure S15**) and *O*-$PtCo_3$/C (**Figure S16**) before and after long-term stability test, and compare their $E_{1/2}$ attenuation as shown in **Figure 4f**. The comparison on ORR activity loss indicates that both ordering and encapsulation make substantial contribution to the enhanced ORR stability. However, contrary to previous works,[34, 36] the SMSI seems to

have limited influence on ORR stability in this work. This is because the positive effect of SMSI may be largely offset by the hampered mass transfer process in *O*-$PtCo_3$/HNCS. Based on above discussion, we deduce that the enhanced ORR stability could be attributed to the following two factors: 1) Carbon encapsulation, which largely prevents the aggregation, detachment and metal dissolution, especially for the Co element with more negative redox potential (Co^{2+}/Co (-0.28 V)). 2) Structure ordering, with unique crystal structure and stronger metal interaction making alloy highly anti-corrosive in acid electrolytes. On the other hand, even though SMSI seems to have a limited effect in the contrast group of *O*-$PtCo_3$/HNCS and *O*-$PtCo_3$/C, its contribution to the enhanced ORR stability of *O*-$PtCo_3$@HNCS cannot be excluded due to the close contact between the N-doped carbon shell and $PtCo_3$ nanoparticles, and the distinct porous structure of carbon support.

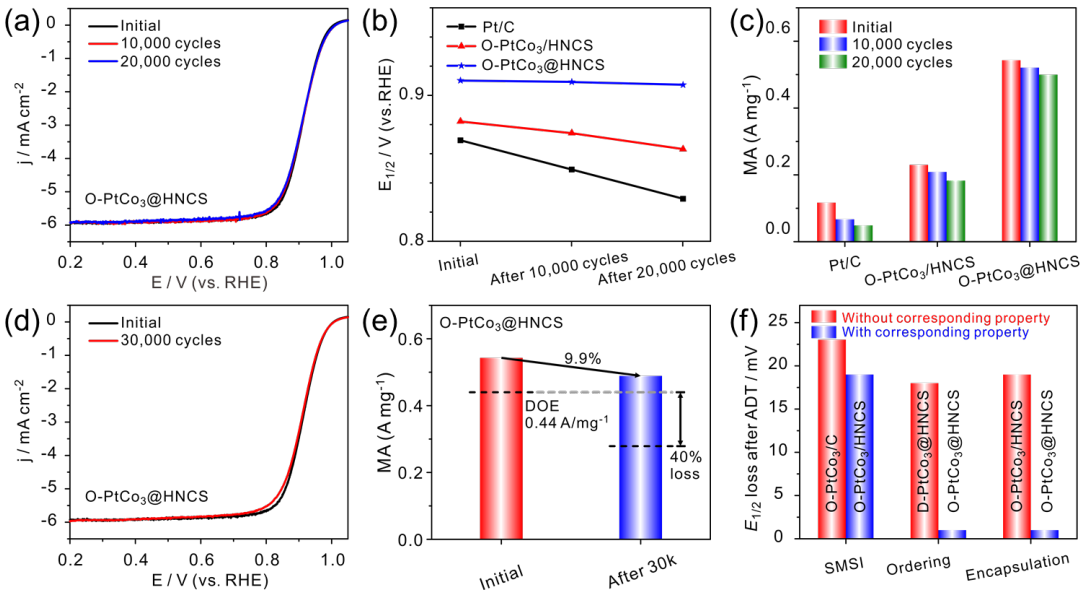

Figure 4. Electrocatalytic stability test at room temperature for different potential cycles. (a) LSV curves of *O*-$PtCo_3$@HNCS. Comparison of the half-wave potentials (b), MA (c) before and after 10,000 and 20,000 potential cycles. (d-e) ORR stability of

O-$PtCo_3$@HNCS compared with DOE target value. (f) Semi-qualitative evaluation on the impact of SMSI, ordering and encapsulation on ORR stability.

The evolution of surface structure was determined by CO stripping voltammetry, which is a sensitive tool to identify the surface adsorption property and track the growth of nanoparticles. **Figure 5a-b and Figure S17** show the CO stripping curves of *O*-$PtCo_3$@HNCS, *O*-$PtCo_3$/HNCS and *O*-$PtCo_3$/C before and after stability test. Before cycling, only one CO oxidation peak (labelled as peak 1) located at around 0.79 V can be observed for *O*-$PtCo_3$@HNCS and *O*-$PtCo_3$/HNCS, while a positive shift (~47 mV) of peak 1 can be seen for *O*-$PtCo_3$/C, which can be attributed to the weakened CO adsorption caused by the SMSI effect in *O*-$PtCo_3$@HNCS and *O*-$PtCo_3$/HNCS [37]. Notably, a shoulder peak (labelled as peak 2) located at 0.736 V can be seen in *O*-$PtCo_3$/C, which may be attributed to the uneven size distribution of nanoparticles caused by the weak interaction between *O*-$PtCo_3$ nanoparticles and carbon black. Thus serious particles growth happens during high-temperature ordering process, as evidenced in **Figure S4**. After the stability test, *O*-$PtCo_3$/HNCS and *O*-$PtCo_3$/C catalysts both exhibit two split CO oxidation peaks (labelled as peak 2 and peak 3, Figure **5b** and Figure **S17**), reflecting inhomogeneous particle sizes. Peak 3 may be attributed to the particle growth during the electrochemical potential cycling, largely caused by particle migration and/or aggregation. Significantly, this peak splitting can hardly be seen in *O*-$PtCo_3$@HNCS, reflecting the protective effect of 'carbon armor' on inhibiting the degradation process. Even so, the additional CO oxidation peaks with positive shifts can be seen for all catalysts, largely due to formation of the favorable Pt-

rich shell during cycling [11]. Above results further reveal the mechanism of stability enhancement by carbon encapsulation. TEM images of *O*-$PtCo_3$@HNCS and *O*-$PtCo_3$/HNCS obtained after stability tests also supported above explanation (**Figure 5c-d**). A uniform size distribution can still be observed for *O*-$PtCo_3$@HNCS and all nanoparticles are well isolated without obvious aggregation. By contrast, severe aggregation happens in *O*-$PtCo_3$/HNCS after stability test **(Figure 5e-f)**. To track the structure evolution of catalysts, XRD patterns of *O*-$PtCo_3$/HNCS and *O*-$PtCo_3$@HNCS before and after stability tests are compared (**Figure S18**). Both samples maintain an ordered structure even after long-term stability tests in corrosive environment. A slight negative shift in 2θ for (111) plane can be detected for *O*-$PtCo_3$/HNCS, while the position for *O*-$PtCo_3$@HNCS does not show obvious change. This indicates considerable leaching of Co in *O*-$PtCo_3$/HNCS, which is another major reason for the attenuated ORR performance in addition to particle growth. These results suggest that carbon encapsulation can both hamper the movement of nanoparticles on the support and simultaneously slow down the leaching of vulnerable metals, which could be critical for the improved ORR stability.

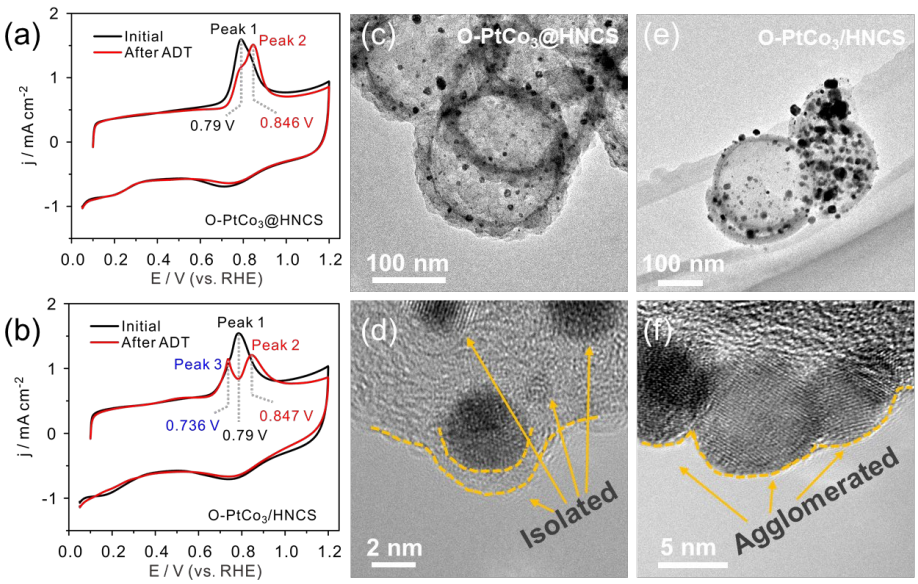

Figure 5. Electrochemical and TEM studies of the surface structure and morphology change before and after stability test. CO stripping curves of (a) *O*-$PtCo_3$@HNCS and (b) *O*-$PtCo_3$/HNCS in Ar-saturated 0.1 M $HClO_4$ solution before and after stability test. TEM images at different magnifications of (c-d) *O*-$PtCo_3$@HNCS and (e-f) *O*-$PtCo_3$/HNCS.

Conclusion

In summary, structurally ordered $PtCo_3$ nanoparticles confined in hollow N-doped carbon sphere were successfully achieved. The hollow N-doped carbon shell serves as a protective 'armor', which not only inhabits the sintering during high-temperature ordering but also inhibits the aggregation, agglomeration and metal leaching during electrochemical potential cycling. Besides, benefiting from the unique mesopore-dominated structure, accelerated mass transfer associated with enhanced activity can be achieved. The substantially enhanced ORR stability, as the first indicator, proves the effective encapsulation as experimentally revealed by TEM and BSE-STEM imaging. Systematic electrochemical stability tests indicate that both the ordered structure and

carbon encapsulation should be mainly responsible for enhanced ORR activity and durability. While ordering could allow *O*-$PtCo_3$/C nanoparticles to approach the predictive volcano peak compared with Pt/C, N-doped carbon encapsulation could make necessary compensation for the excessively weakened OH adsorption as confirmed by XPS. The preliminary findings may pave the way for understanding the encapsulation strategy in depth and designing low-cost catalysts with both high activity and stability for various applications.

Supporting information

The Supporting Information is available free of charge on the ACS Publications website at DOI:

Material preparation, Test Parameters, HRTEM, comparison of XRD, morphology, defects, stability test. (PDF).

Author information

Corresponding Authors

*E-mail: yezhu@polyu.edu.hk

*E-mail: wangdl81125@hust.edu.cn

Acknowledgements

This work was financially supported by the National Natural Science Foundation (91963109), the Research Grants Council of Hong Kong (Project no. C5029-18E) and the Hong Kong Polytechnic University grant (No. ZVRP). The authors thank the Analytical and Testing Center of HUST for allowing the use of its help and facilities for XRD and XPS.

References

(1) Stephens, I. E. L.; Rossmeisl, J.; Chorkendorff, I. Toward sustainable fuel cells. *Science* **2016**, *354* (6318), 1378-1379. DOI: https://doi.org/doi:10.1126/science.aal3303.

(2) Wang, M.-Q.; Yang, W.-H.; Wang, H.-H.; Chen, C.; Zhou, Z.-Y.; Sun, S.-G. Pyrolyzed Fe–N–C Composite as an Efficient Non-precious Metal Catalyst for Oxygen Reduction Reaction in Acidic Medium. *ACS Catal.* **2014**, *4* (11), 3928-3936. DOI: https://doi.org/10.1021/cs500673k.

(3) He, Y.; Hwang, S.; Cullen, D. A.; Uddin, M. A.; Langhorst, L.; Li, B.; Karakalos, S.; Kropf, A. J.; Wegener, E. C.; Sokolowski, J.; et al. Highly active atomically dispersed CoN4 fuel cell cathode catalysts derived from surfactant-assisted MOFs: carbon-shell confinement strategy. *Energy Environ. Sci.* **2019**, *12* (1), 250-260. DOI: https://doi.org/10.1039/c8ee02694g.

(4) Wang, Z.; Jin, H.; Meng, T.; Liao, K.; Meng, W.; Yang, J.; He, D.; Xiong, Y.; Mu, S. Fe, Cu-Coordinated ZIF-Derived Carbon Framework for Efficient Oxygen Reduction Reaction and Zinc–Air Batteries. *Adv. Funct. Mater.* **2018**, *28* (39), 1802596. DOI: https://doi.org/10.1002/adfm.201802596.

(5) Singh, S. K.; Takeyasu, K.; Nakamura, J. Active Sites and Mechanism of Oxygen Reduction Reaction Electrocatalysis on Nitrogen-Doped Carbon Materials. *Adv. Mater.* **2018**, *31*, 1804297. DOI: https://doi.org/10.1002/adma.201804297.

(6) Liang, H. W.; Wei, W.; Wu, Z. S.; Feng, X.; Mullen, K. Mesoporous metal-nitrogen-doped carbon electrocatalysts for highly efficient oxygen reduction reaction. *J. Am. Chem. Soc.* **2013**, *135* (43), 16002-16005. DOI: https://doi.org/10.1021/ja407552k.

(7) Du, L.; Prabhakaran, V.; Xie, X.; Park, S.; Wang, Y.; Shao, Y. Low-PGM and PGM-Free Catalysts for Proton Exchange Membrane Fuel Cells: Stability Challenges and Material Solutions. *Adv. Mater.* **2021**, *33* (6), 1908232. DOI: https://doi.org/https://doi.org/10.1002/adma.201908232.

(8) Choi, J.; Lee, Y. J.; Park, D.; Jeong, H.; Shin, S.; Yun, H.; Lim, J.; Han, J.; Kim, E. J.; Jeon, S. S.; et al. Highly Durable Fuel Cell Catalysts Using Crosslinkable Block

Copolymer-Based Carbon Supports with Ultralow Pt Loadings. *Energy Environ. Sci.* **2020**, *13* (12), 4921-4929. DOI: https://doi.org/10.1039/D0EE01095B.

(9) Stamenkovic, V. R.; Fowler, B.; Mun, B. S.; Wang, G.; Ross, P. N.; Lucas, C. A.; Marković, N. M. Improved Oxygen Reduction Activity on Pt₃Ni(111) via Increased Surface Site Availability. *Science* **2007**, *315* (5811), 493-497. DOI: https://doi.org/doi:10.1126/science.1135941.

(10) Oezaslan, M.; Hasché, F.; Strasser, P. Oxygen Electroreduction on PtCo3, PtCo and Pt3Co Alloy Nanoparticles for Alkaline and Acidic PEM Fuel Cells. *J. Electrochem. Soc.* **2012**, *159* (4), B394-B405. DOI: https://doi.org/10.1149/2.075204jes.

(11) Wang, Z.; Yao, X.; Kang, Y.; Miao, L.; Xia, D.; Gan, L. Structurally Ordered Low-Pt Intermetallic Electrocatalysts toward Durably High Oxygen Reduction Reaction Activity. *Adv. Funct. Mater.* **2019**, *29* (35), 1902987. DOI: https://doi.org/10.1002/adfm.201902987.

(12) Wu, Z.-P.; Caracciolo, D. T.; Maswadeh, Y.; Wen, J.; Kong, Z.; Shan, S.; Vargas, J. A.; Yan, S.; Hopkins, E.; Park, K.; et al. Alloying–realloying enabled high durability for Pt–Pd-3d-transition metal nanoparticle fuel cell catalysts. *Nat. Commun.* **2021**, *12* (1), 859. DOI: https://doi.org/10.1038/s41467-021-21017-6.

(13) Liang, J.; Zhao, Z.; Li, N.; Wang, X.; Li, S.; Liu, X.; Wang, T.; Lu, G.; Wang, D.; Hwang, B.-J.; et al. Biaxial Strains Mediated Oxygen Reduction Electrocatalysis on Fenton Reaction Resistant L10-PtZn Fuel Cell Cathode. *Adv. Energy Mater.* **2020**, *10* (29), 2000179. DOI: https://doi.org/10.1002/aenm.202000179.

(14) Wang, D.; Xin, H. L.; Hovden, R.; Wang, H.; Yu, Y.; Muller, D. A.; DiSalvo, F. J.; Abruña, H. D. Structurally ordered intermetallic platinum–cobalt core–shell nanoparticles with enhanced activity and stability as oxygen reduction electrocatalysts. *Nat. Mater.* **2012**, *12*, 81-87. DOI: https://doi.org/10.1038/nmat3458.

(15) Wang, T.; Liang, J.; Zhao, Z.; Li, S.; Lu, G.; Xia, Z.; Wang, C.; Luo, J.; Han, J.; Ma, C.; et al. Sub-6 nm Fully Ordered L10-Pt–Ni–Co Nanoparticles Enhance Oxygen Reduction via Co Doping Induced Ferromagnetism Enhancement and Optimized Surface Strain. *Adv. Energy Mater.* **2019**, *9* (17), 1803771. DOI: https://doi.org/10.1002/aenm.201803771.

(16) Hu, Y.; Lu, Y.; Zhao, X.; Shen, T.; Zhao, T.; Gong, M.; Chen, K.; Lai, C.; Zhang, J.; Xin, H. L.; et al. Highly active N-doped carbon encapsulated Pd-Fe intermetallic nanoparticles for the oxygen reduction reaction. *Nano Res.* **2020**, *13*, 2365-2370. DOI: https://doi.org/10.1007/s12274-020-2856-z.

(17) Zhao, W.; Ye, Y.; Jiang, W.; Li, J.; Tang, H.; Hu, J.; Du, L.; Cui, Z.; Liao, S. Mesoporous carbon confined intermetallic nanoparticles as highly durable electrocatalysts for the oxygen reduction reaction. *J. Mater. Chem. A* **2020**, *8* (31), 15822-15828. DOI: https://doi.org/10.1039/D0TA01437K.

(18) Perez-Alonso, F. J.; Elkjær, C. F.; Shim, S. S.; Abrams, B. L.; Stephens, I. E. L.; Chorkendorff, I. Identical locations transmission electron microscopy study of Pt/C electrocatalyst degradation during oxygen reduction reaction. *J. Power Sources* **2011**, *196* (15), 6085-6091. DOI: https://doi.org/10.1016/j.jpowsour.2011.03.064.

(19) Meier, J. C.; Katsounaros, I.; Galeano, C.; Bongard, H. J.; Topalov, A. A.; Kostka, A.; Karschin, A.; Schüth, F.; Mayrhofer, K. J. J. Stability investigations of electrocatalysts on the nanoscale. *Energy Environ. Sci.* **2012**, *5* (11), 9319-9330. DOI: https://doi.org/10.1039/C2EE22550F.

(20) Deng, D.; Yu, L.; Chen, X.; Wang, G.; Jin, L.; Pan, X.; Deng, J.; Sun, G.; Bao, X. Iron encapsulated within pod-like carbon nanotubes for oxygen reduction reaction. *Angew. Chem. Int. Ed.* **2013**, *52* (1), 371-375. DOI: https://doi.org/10.1002/anie.201204958.

(21) Hu, Y.; Shen, T.; Zhao, X.; Zhang, J.; Lu, Y.; Shen, J.; Lu, S.; Tu, Z.; Xin, H. L.; Wang, D. Combining structurally ordered intermetallics with N-doped carbon confinement for efficient and anti-poisoning electrocatalysis. *Appl. Catal. B* **2020**, *279*, 119370. DOI: https://doi.org/10.1016/j.apcatb.2020.119370.

(22) Galeano, C.; Meier, J. C.; Peinecke, V.; Bongard, H.; Katsounaros, I.; Topalov, A. A.; Lu, A.; Mayrhofer, K. J. J.; Schüth, F. Toward Highly Stable Electrocatalysts via Nanoparticle Pore Confinement. *J. Am. Chem. Soc.* **2012**, *134* (50), 20457-20465. DOI: https://doi.org/10.1021/ja308570c.

(23) Karuppannan, M.; Kim, Y.; Gok, S.; Lee, E.; Hwang, J. Y.; Jang, J.-H.; Cho, Y.-H.; Lim, T.; Sung, Y.-E.; Kwon, O. J. A highly durable carbon-nanofiber-supported Pt–C

core–shell cathode catalyst for ultra-low Pt loading proton exchange membrane fuel cells: facile carbon encapsulation. *Energy Environ. Sci.* **2019**, *12* (9), 2820-2829. DOI: https://doi.org/10.1039/C9EE01000A.

(24) Hu, Y.; Zhang, J.; Shen, T.; Li, Z.; Chen, K.; Lu, Y.; Zhang, J.; Wang, D. Efficient Electrochemical Production of H2O2 on Hollow N-Doped Carbon Nanospheres with Abundant Micropores. *ACS Appl. Mat. Interfaces* **2021**, *13* (25), 29551-29557. DOI: https://doi.org/10.1021/acsami.1c05353.

(25) Wang, T.; He, Y.; Liu, Y.; Guo, F.; Li, X.; Chen, H.; Li, H.; Lin, Z. A ZIF-triggered rapid polymerization of dopamine renders Co/N-codoped cage-in-cage porous carbon for highly efficient oxygen reduction and evolution. *Nano Energy* **2021**, *79*, 105487. DOI: https://doi.org/10.1016/j.nanoen.2020.105487.

(26) Lu, Y.; Liang, J.; Deng, S.; He, Q.; Deng, S.; Hu, Y.; Wang, D. Hypercrosslinked polymers enabled micropore-dominant N, S Co-Doped porous carbon for ultrafast electron/ion transport supercapacitors. *Nano Energy* **2019**, *65*, 103993. DOI: https://doi.org/10.1016/j.nanoen.2019.103993.

(27) Xiong, Y.; Yang, Y.; DiSalvo, F. J.; Abruña, H. D. Synergistic Bimetallic Metallic Organic Framework-Derived Pt–Co Oxygen Reduction Electrocatalysts. *ACS Nano* **2020**, *14* (10), 13069-13080. DOI: https://doi.org/10.1021/acsnano.0c04559.

(28) Su, C.-Y.; Cheng, H.; Li, W.; Liu, Z.-Q.; Li, N.; Hou, Z.; Bai, F.-Q.; Zhang, H.-X.; Ma, T.-Y. Atomic Modulation of FeCo-Nitrogen-Carbon Bifunctional Oxygen Electrodes for Rechargeable and Flexible All-Solid-State Zinc-Air Battery. *Adv. Energy Mater.* **2017**, *7* (13), 1602420. DOI: https://doi.org/10.1002/aenm.201602420.

(29) Wang, Y.; Wang, L.; Tong, M.; Zhao, X.; Gao, Y.; Fu, H. Co-VN encapsulated in bamboo-like N-doped carbon nanotubes for ultrahigh-stability of oxygen reduction reaction. *Nanoscale* **2018**, *10* (9), 4311-4319. DOI: https://doi.org/10.1039/c7nr09538d.

(30) Gao, Y.; Peng, H.; Wang, Y.; Wang, G.; Xiao, L.; Lu, J.; Zhuang, L. Improving the Antioxidation Capability of the Ni Catalyst by Carbon Shell Coating for Alkaline Hydrogen Oxidation Reaction. *ACS Appl. Mat. Interfaces* **2020**, *12* (28), 31575-31581. DOI: https://doi.org/10.1021/acsami.0c10784.

(31) Deng, Z.; Pang, W.; Gong, M.; Jin, Z.; Wang, X. Revealing the role of mo doping

in promoting oxygen reduction reaction performance of Pt3Co nanowires. *J. Energy Chem.* **2022**, *66*, 16-23. DOI: https://doi.org/10.1016/j.jechem.2021.06.018.

(32) Kulkarni, A.; Siahrostami, S.; Patel, A.; Nørskov, J. K. Understanding Catalytic Activity Trends in the Oxygen Reduction Reaction. *Chem. Rev.* **2018**, *118* (5), 2302-2312. DOI: https://doi.org/10.1021/acs.chemrev.7b00488.

(33) Ferrero, G. A.; Fuertes, A. B.; Sevilla, M.; Titirici, M.-M. Efficient metal-free N-doped mesoporous carbon catalysts for ORR by a template-free approach. *Carbon* **2016**, *106*, 179-187. DOI: https://doi.org/10.1016/j.carbon.2016.04.080.

(34) Qiao, Z.; Hwang, S.; Li, X.; Wang, C.; Samarakoon, W.; Karakalos, S.; Li, D.; Chen, M.; He, Y.; Wang, M.; et al. 3D porous graphitic nanocarbon for enhancing the performance and durability of Pt catalysts: a balance between graphitization and hierarchical porosity. *Energy Environ. Sci.* **2019**, *12* (9), 2830-2841, 10.1039/C9EE01899A. DOI: https://doi.org/10.1039/C9EE01899A.

(35) Jang, J.-H.; Jeffery, A. A.; Min, J.; Jung, N.; Yoo, S. J. Emerging carbon shell-encapsulated metal nanocatalysts for fuel cells and water electrolysis. *Nanoscale* **2021**, *13* (36), 15116-15141. DOI: https://doi.org/10.1039/D1NR01328A.

(36) Han, X.; Cheng, F.; Zhang, T.; Yang, J.; Hu, Y.; Chen, J. Hydrogenated Uniform Pt Clusters Supported on Porous CaMnO3 as a Bifunctional Electrocatalyst for Enhanced Oxygen Reduction and Evolution. *Adv. Mater.* **2014**, *26* (13), 2047-2051. DOI: https://doi.org/10.1002/adma.201304867.

(37) Robinson, J. E.; Labrador, N. Y.; Chen, H.; Sartor, B. E.; Esposito, D. V. Silicon Oxide-Encapsulated Platinum Thin Films as Highly Active Electrocatalysts for Carbon Monoxide and Methanol Oxidation. *ACS Catal.* **2018**, *8* (12), 11423-11434. DOI: https://doi.org/10.1021/acscatal.8b03626.

For Table of Contents Only